

Gravitational waves from a test particle scattered by a neutron star: Axial mode case

Kazuhiro Tominaga^{1 *}, Motoyuki Saijo^{1 †}, and Kei-ichi Maeda^{1,2 ‡}

¹ *Department of Physics, Waseda University, 3-4-1 Okubo, Shinjuku, Tokyo 169-8555, Japan*

² *Advanced Research Institute for Science and Engineering,
Waseda University, Shinjuku, Tokyo 169-8555, Japan*

(October 21, 2018)

Using a metric perturbation method, we study gravitational waves from a test particle scattered by a spherically symmetric relativistic star. We calculate the energy spectrum and the waveform of gravitational waves for axial modes. Since metric perturbations in axial modes do not couple to the matter fluid of the star, emitted waves for a normal neutron star show only one peak in the spectrum, which corresponds to the orbital frequency at the turning point, where the gravitational field is strongest. However, for an ultracompact star (the radius $R \lesssim 3M$), another type of resonant periodic peak appears in the spectrum. This is just because of an excitation by a scattered particle of axial quasinormal modes, which were found by Chandrasekhar and Ferrari. This excitation comes from the existence of the potential minimum inside of a star. We also find for an ultracompact star many small periodic peaks at the frequency region beyond the maximum of the potential, which would be due to a resonance of two waves reflected by two potential barriers (Regge-Wheeler type and one at the center of the star). Such resonant peaks appear neither for a normal neutron star nor for a Schwarzschild black hole. Consequently, even if we analyze the energy spectrum of gravitational waves only for axial modes, it would be possible to distinguish between an ultracompact star and a normal neutron star (or a Schwarzschild black hole).

PACS number(s): 04.25.Nx, 04.30.-w, 04.40.Dg

I. INTRODUCTION

A laser interferometer to detect gravitational waves, such as the Laser Interferometric Gravitational Wave Observatory (LIGO), VIRGO, GEO600, or TAMA300, will be in operation within several years [1]. It is one of the most urgent subjects for theoretical relativists to make a set of templates of gravitational waves. The direct detection of gravitational waves is very important not only as a new “eye” observing the Universe (gravitational wave astronomy) but also as a new probe for fundamental physics. For example, we know that a neutron star, which is observed as a pulsar, has a mass $M \approx 1.4M_{\odot}$ and a radius $R \approx 10$ km. Although we can guess its central region with some theoretical ansatz, we have no direct information from the inside of a neutron star because neither radiation nor a neutrino is transparent in the central region. The direct detection of gravitational waves may provide some information about the inside of a neutron star when it is formed, resulting in new observational facts or constraints about the equation of state for high density matter.

One of the most promising astronomical sources for these ground-based detectors is a coalesced compact binary such as a neutron star binary. To complete a set of templates from such a source, many studies about the emitted gravitational waves have been done using various techniques.

A numerical simulation without approximations (numerical relativity) is probably one of the best ways to calculate gravitational waves emitted from the compact binary system [2,3]. Although steady progress in numerical relativity has been achieved, there are still some difficulties which prevent us from finding the final results.

Instead, there are some powerful approximation methods to mimic the coalescence of a compact binary system. One such approximation is the perturbative approach. Regge and Wheeler [4] and Zerilli [5] first formulated a method for metric perturbations in a Schwarzschild black hole spacetime. Then there are many works using such a black hole perturbation method in which we describe gravitational waves by metric perturbations in a black hole background spacetime and treat a companion of the binary as a test particle [6–8]. This approximation for gravitational waves in a head-on collision of two black holes gives a good agreement with the results obtained by numerical simulation

*Electronic address: tominaga@gravity.phys.waseda.ac.jp

†Electronic address: saiyo@gravity.phys.waseda.ac.jp

‡Electronic address: maeda@gravity.phys.waseda.ac.jp

[9]. Thus, such a perturbative approach may provide a good approximation for gravitational waves from a compact binary as well.

However, there are so far few works for neutron star perturbations. One may think that if we have two $1.4M_{\odot}$ neutron stars, it will be a black hole after coalescence, when the ringing tail of the gravitational waves can be described by quasinormal modes of the black hole. The quasinormal modes of a neutron star may have nothing to do with the final stage of the coalescence. However, before black hole formation, we have to analyze the orbital evolution of the neutron star binary. Therefore, we believe that a perturbation analysis for a neutron star is also important.

For a nonradial pulsation of a spherically symmetric relativistic star, perturbation equations both for axial and polar modes were first derived by Thorne and Campolattaro [10]. Similar to the black hole perturbation, the axial mode for a spherical star is described by a second order differential equation. On the other hand, the polar mode was first described by a fifth order differential equation [10]. However, because of the dynamical degrees of freedom of polar modes, i.e., sound waves and gravitational waves, the basic equation can be reduced to a fourth order differential equation as shown by Lindblom and Detweiler [11]. Lindblom, Mendell, and Ipser [12] also derived a couple of second order differential equations, which could be interpreted as those for sound waves and gravitational waves, respectively.

As in the case of black hole perturbations, quasinormal modes, if they exist, will be important in the analysis of gravitational waves from a compact binary. For the polar mode, there are two types of quasinormal modes of a neutron star; one is a fluid oscillation mode similar to the f , p , g modes of a Newtonian star (cf. [13]); the other is a wave mode (w mode), which exists only in general relativity [14–18]. Even for the axial mode, Chandrasekhar and Ferrari [19] illustrated that quasinormal modes exist if the effective potential has a minimal as that in an ultracompact star. Kokkotas [20] numerically calculated such axial quasinormal modes for various ultracompact stars. Kojima [21] extended it to a slowly rotating star, setting Regge-Wheeler gauge conditions.

As for emitted gravitational waves from a binary system, Kojima [22] studied them for the case that a test particle is moving in a circular orbit around a polytropic star. For a circular orbit, the axial mode cancels from the orbital symmetry so that the polar mode was only taken into account. He showed that the resonance mode appears in the energy flux when the orbit reaches the radius where the orbital frequency coincides with that of the quasinormal mode. For the axial mode, recently, Borrelli [23] calculated energy spectra of gravitational waves emitted by a test particle spiraling into an ultracompact star. In his result, its energy spectrum shows many peaks, which correspond to axial quasinormal modes of the star. Although it is important, since we are interested in a compact binary, a direct collision might show some different features from the binary case. We also do not know what will happen when a test particle reaches the surface of the star. To avoid such an unknown factor and to analyze the case of a compact binary, we first study gravitational waves emitted when a test particle is scattered by a neutron star in this paper.

For a Schwarzschild black hole, Oohara and Nakamura [8] analyzed it and showed that the energy spectrum has no peak except for one which corresponds to the orbital frequency. Here we consider a spherical star instead of a Schwarzschild black hole. We study only the axial mode which does not exist in Newton gravity. To discuss the dependence of the equations of state, we analyze two models: a uniform density star as in [19,20,23] and a polytropic star.

This paper is organized as follows. In Secs. IIA and IIB, we briefly review the perturbation theory for a spherically symmetric relativistic star. We show our numerical results in Sec. III. Section IV is devoted to a discussion. Some numerical techniques for calculating gravitational waves are summarized in the Appendix. Throughout this paper, we use units of $c = G = 1$ and a metric signature of $(-, +, +, +)$.

II. LINEARIZED EINSTEIN EQUATIONS: AXIAL MODES

We start with summarizing briefly the metric perturbation of a spherically symmetric relativistic star. A spherically symmetric background metric $g_{\mu\nu}^{(0)}$ is described as

$$ds^2 = g_{\mu\nu}^{(0)} dx^{\mu} dx^{\nu} = -e^{\nu(r)} dt^2 + e^{\lambda(r)} dr^2 + r^2 (d\theta^2 + \sin^2 \theta d\phi^2), \quad (2.1)$$

$$e^{-\lambda(r)} = 1 - \frac{2M(r)}{r}, \quad (2.2)$$

where $M(r)$ is a mass function inside a radius r . We assume a perfect fluid as the stellar matter, i.e.

$$T^{\mu\nu} = (\rho + P)u^{\mu}u^{\nu} + Pg^{\mu\nu}, \quad (2.3)$$

where ρ and P are the total energy density and the pressure, respectively, which satisfy a barotropic equation of state, $P = P(\rho)$. Using Tolman-Oppenheimer-Volkov equations, we construct a stellar model and its spacetime

metric numerically except for the constant density star case. The radius R of a star is defined by a surface where the pressure vanishes, and the mass of the star M is given by $M = M(R)$.

For linearized Einstein equations, we can decompose the perturbed metric into an axial mode $h_{\mu\nu}^{(\text{axial})}$ and a polar mode $h_{\mu\nu}^{(\text{polar})}$:

$$g_{\mu\nu} = g_{\mu\nu}^{(0)} + h_{\mu\nu}^{(\text{axial})} + h_{\mu\nu}^{(\text{polar})}. \quad (2.4)$$

Using Regge-Wheeler gauge conditions, we will integrate the interior and exterior regions of the linearized Einstein equations, separately, and impose appropriate junction conditions at the surface R to find the solution. In this paper, we only deal with axial mode perturbation. Then, we write down the linearized Einstein equation only for axial modes in the following subsections.

A. Interior region of the star

In order to find the linearized Einstein equations for axial modes, we expand the perturbed metric by tensor harmonics for polar angle θ and azimuthal angle ϕ [5], and proceed to a Fourier transformation for the time coordinate t . Although there are ten independent components for the linearized metric, four of them are gauge freedoms of coordinate transformations, which are fixed by a choice of Regge-Wheeler gauge [4], resulting in two components belonging to axial modes, while the rest of the four correspond to polar modes. For axial mode perturbations, we can set

$$\begin{aligned} h_{\mu\nu}^{(\text{axial})} dx^\mu dx^\nu = & \frac{1}{2\pi} \int d\omega \sum_{l,m} 2h_{0,l}(r) \left(-\frac{1}{\sin\theta} \frac{\partial Y_{lm}}{\partial\phi} dt d\theta + \sin\theta \frac{\partial Y_{lm}}{\partial\theta} dt d\phi \right) e^{-i\omega t} \\ & + \frac{1}{2\pi} \int d\omega \sum_{l,m} 2h_{1,l}(r) \left(-\frac{1}{\sin\theta} \frac{\partial Y_{lm}}{\partial\phi} dr d\theta + \sin\theta \frac{\partial Y_{lm}}{\partial\theta} dr d\phi \right) e^{-i\omega t}, \end{aligned} \quad (2.5)$$

where $h_{0,l}$ and $h_{1,l}$ are functions of the radial coordinate r defined below, and $Y_{lm}(\theta, \phi)$ is a spherical harmonics.

The axial mode in the interior region of a star is described by a single wave equation for gravitational waves, because a rotation does not exist in a spherically symmetric background spacetime. That is, we have a single wave function $X_{l\omega}^{(\text{int})}$, which determines the behaviors of axial modes as

$$h_{1,l,\omega} = e^{-(\nu-\lambda)/2} r X_{l\omega}^{(\text{int})}, \quad (2.6)$$

$$h_{0,l,\omega} = \frac{i}{\omega} e^{(\nu-\lambda)/2} \frac{d}{dr} \left(r X_{l\omega}^{(\text{int})} \right). \quad (2.7)$$

The equation for the wave function $X_{l\omega}^{(\text{int})}$ is derived from the linearized Einstein equation for axial modes as

$$\frac{d^2 X_{l\omega}^{(\text{int})}}{dr^{*2}} + \left(\omega^2 - V_l^{(\text{int})} \right) X_{l\omega}^{(\text{int})} = 0, \quad (2.8)$$

where the ‘‘tortoise’’ coordinate r^* and the effective potential $V_l^{(\text{int})}$ are defined as

$$r^* = \int_0^r e^{-(\nu-\lambda)/2} dr, \quad (2.9)$$

$$V_l^{(\text{int})} = e^\nu \left(\frac{l(l+1)}{r^2} - \frac{6M(r)}{r^3} - 4\pi(P - \rho) \right), \quad (2.10)$$

respectively.

As for the boundary condition, the wave function $X_{l\omega}^{(\text{int})}$ must be regular at the center of a star. Expanding $X_{l\omega}^{(\text{int})}$ around the center $r = 0$, we find

$$X_{l\omega}^{(\text{int})} = \eta_{l\omega} \left\{ r^{l+1} + \frac{1}{2(2l+3)} \left[4\pi(l+2) \left(\frac{1}{3}(2l-1)\rho_c - P_c \right) - \omega^2 e^{-\nu_c} \right] r^{l+3} + O(r^{l+5}) \right\}, \quad (2.11)$$

where $\eta_{l\omega}$ is an arbitrary constant, and ρ_c , P_c , and ν_c are the central density, pressure, and metric functions, respectively.

Apart from a free parameter $\eta_{l\omega}$, we obtain a solution $X_{l\omega}^{(\text{int})}$ by integrating Eq. (2.8) with the boundary condition (2.11). Further details of the numerical techniques constructing the wave function $X_{l\omega}^{(\text{int})}$ are given in the Appendix, subsection A 1.

B. Exterior region of the star

The background metric outside the star is the Schwarzschild spacetime, i.e. , Eq. (2.1), with

$$e^\nu = e^{-\lambda} = 1 - \frac{2M}{r}. \quad (2.12)$$

As for the trajectory of a test particle, without loss of generality, we can assume that the particle moves on the equatorial plane ($\theta = \pi/2$). Then, the equation of motion for the particle is described as

$$\frac{d\hat{T}}{d\tau} = \tilde{E} / \left(1 - \frac{2M}{\hat{R}}\right), \quad (2.13)$$

$$\left(\frac{d\hat{R}}{d\tau}\right)^2 = \tilde{E}^2 - \left(1 - \frac{2M}{\hat{R}}\right) \left(1 + \frac{\tilde{L}^2}{\hat{R}^2}\right), \quad (2.14)$$

$$\hat{\Theta} = \frac{\pi}{2}, \quad (2.15)$$

$$\frac{d\hat{\Phi}}{d\tau} = \frac{\tilde{L}}{\hat{R}^2}, \quad (2.16)$$

where the particle trajectory is $Z^\mu = (\hat{T}(\tau), \hat{R}(\tau), \hat{\Theta}(\tau), \hat{\Phi}(\tau))$, and μ , \tilde{E} , and \tilde{L} are the mass, the normalized energy, and the normalized orbital angular momentum of the particle, respectively, with $\tilde{E} = E/\mu$ and $\tilde{L} = L/\mu$. The normalized effective potential energy $\tilde{V}^{(\text{particle})}(r)$ of the particle is given as

$$\tilde{V}^{(\text{particle})}(r) = \sqrt{\left(1 - \frac{2M}{r}\right) \left(1 + \frac{\tilde{L}^2}{r^2}\right)}. \quad (2.17)$$

In this paper, since we only consider the motion of a test particle scattered by a spherical star, the particle orbit is unbounded, i.e.,

$$|\tilde{L}|/M > 4, \quad 1 \leq \tilde{E} < \tilde{V}_{\text{max}}^{(\text{particle})}, \quad (2.18)$$

where $\tilde{V}_{\text{max}}^{(\text{particle})}$ is the maximum value of the potential.

The perturbed metric outside a star only comes from an oscillation of spacetime, that is, gravitational waves. Then, similar to the interior region, the linearized Einstein equations for the metric $h_{1,lm}$ and $h_{0,lm}$ defined as Eq. (2.5) are reduced to a single wave equation for a new wave function $X_{lm\omega}^{(\text{ext})}$ defined by

$$h_{1,lm\omega} = e^\lambda r X_{lm\omega}^{(\text{ext})}, \quad (2.19)$$

$$h_{0,lm\omega} = \frac{i}{\omega} e^{-\lambda} \frac{d}{dr} \left(r X_{lm\omega}^{(\text{ext})} \right) - \frac{8\pi i}{\omega} \frac{r^2 e^{-\lambda}}{\sqrt{2n(n+1)}} D_{lm}(\omega, r), \quad (2.20)$$

where $n \equiv (l-1)(l+2)/2$ and $D_{lm}(\omega, r)$ is one of the source terms given below.

From the linearized vacuum Einstein equations, we find the wave equation for $X_{lm\omega}^{(\text{ext})}$ (Regge-Wheeler equation) [4] as

$$\frac{d^2 X_{lm\omega}^{(\text{ext})}}{dr^{*2}} + \left(\omega^2 - V_l^{(\text{ext})}\right) X_{lm\omega}^{(\text{ext})} = S_{lm\omega}^{(\text{ext})}, \quad (2.21)$$

where r^* is the tortoise coordinate defined by

$$r^* = r + 2M \ln \left(\frac{r}{2M} - 1 \right), \quad (2.22)$$

$V_l^{(\text{ext})}$ is Regge-Wheeler potential given by

$$V_l^{(\text{ext})} = e^{-\lambda} \left(\frac{l(l+1)}{r^2} - \frac{6M}{r^3} \right), \quad (2.23)$$

and $S_{lm\omega}^{(\text{ext})}$ is the source term, which is described by the energy-momentum tensor of a test particle expanded by tensor harmonics [5] as

$$S_{lm\omega}^{(\text{ext})} = 8\pi \left[\frac{e^{-2\lambda}}{\sqrt{n+1}} Q_{lm}(\omega, r) + \frac{re^{-\lambda}}{\sqrt{2n(n+1)}} \frac{d}{dr} [e^{-\lambda} D_{lm}(\omega, r)] \right], \quad (2.24)$$

with $Q_{lm}(t, r)$ and $D_{lm}(t, r)$ being

$$Q_{lm}(t, r) = \frac{1}{\sqrt{n+1}} \frac{\mu}{r} e^\lambda \int_{-\infty}^{\infty} d\tau \frac{d\hat{R}}{d\tau} \delta(t - \hat{T}(\tau)) \delta(r - \hat{R}(\tau)) \times \left[\frac{1}{\sin \hat{\Theta}} \frac{\partial \bar{Y}_{lm}}{\partial \hat{\Phi}} \frac{d\hat{\Theta}}{d\tau} - \sin \hat{\Theta} \frac{\partial \bar{Y}_{lm}}{\partial \hat{\Theta}} \frac{d\hat{\Phi}}{d\tau} \right], \quad (2.25)$$

$$D_{lm}(t, r) = -\frac{1}{\sqrt{2n(n+1)}} \mu \int_{-\infty}^{\infty} d\tau \delta(t - \hat{T}(\tau)) \delta(r - \hat{R}(\tau)) \times \left\{ \frac{1}{2} \left[\left(\frac{d\hat{\Theta}}{d\tau} \right)^2 - \sin^2 \hat{\Theta} \left(\frac{d\hat{\Phi}}{d\tau} \right)^2 \right] \frac{1}{\sin \hat{\Theta}} \bar{X}_{lm}(\hat{\Omega}) - \sin \hat{\Theta} \frac{d\hat{\Theta}}{d\tau} \frac{d\hat{\Phi}}{d\tau} \bar{W}_{lm}(\hat{\Omega}) \right\}. \quad (2.26)$$

X_{lm} , W_{lm} are the tensorial part of a tensor harmonics defined by

$$X_{lm} = 2 \frac{\partial}{\partial \phi} \left(\frac{\partial}{\partial \theta} - \cot \theta \right) Y_{lm}, \quad (2.27)$$

$$W_{lm} = \left(\frac{\partial^2}{\partial \theta^2} - \cot \theta \frac{\partial}{\partial \theta} - \frac{1}{\sin^2 \theta} \frac{\partial^2}{\partial \phi^2} \right) Y_{lm}, \quad (2.28)$$

and the overbar denotes the complex conjugate.

The boundary condition outside the star should be imposed such that there is no incoming wave at infinity,

$$X_{lm\omega}^{(\text{ext})} \rightarrow A_{lm\omega} e^{i\omega r^*} \quad (r^* \rightarrow \infty), \quad (2.29)$$

where $A_{lm\omega}$ is the amplitude of an outgoing wave at infinity. The details of constructing the wave function $X_{lm\omega}^{(\text{ext})}$ are given in the Appendix, subsections A 2 and A 3.

C. Matching of two wave functions and gravitational waves

We have to combine two wave functions, the interior wave function $X_{l\omega}^{(\text{int})}$ and the exterior one $X_{lm\omega}^{(\text{ext})}$, at the surface of the star. The matching condition is that the wave function must be continuous and smooth at the surface. For the case of the axial mode, since the wave function inside the star does not couple to perturbations of the matter fluid, the condition turns out to be very simple as

$$X_{l\omega}^{(\text{int})}(R^*) = X_{lm\omega}^{(\text{ext})}(R^*), \quad (2.30)$$

$$\frac{dX_{l\omega}^{(\text{int})}}{dr^*}(R^*) = \frac{dX_{lm\omega}^{(\text{ext})}}{dr^*}(R^*), \quad (2.31)$$

where R^* is the radius of the star by use of the ‘‘tortoise’’ coordinate.

Then we calculate the amplitude of the gravitational waves $A_{lm\omega}$ as follows: We first integrate Eqs. (2.8) and (2.21) using their boundary conditions, Eqs. (2.11) and (2.29). Next, we connect those solutions at the surface of the star using Eqs. (2.30) and (2.31), which determine two unknown coefficients $\eta_{l\omega}$ and $A_{lm\omega}$.

From the wave function obtained as above, we obtain some information about gravitational waves emitted by a scattered particle. When we discuss the gravitational waves, we usually decompose them into two modes: + and ×

modes. Then, we have to transform our coordinate system from the Regge-Wheeler gauge to the transverse-traceless one, which metric near infinity is described as

$$ds^2 = -dt^2 + dr^2 + r^2(1 + h_+)d\theta^2 + r^2 \sin^2 \theta(1 - h_+)d\phi^2 + r^2 \sin \theta h_\times d\theta d\phi. \quad (2.32)$$

Then the axial mode in transverse-traceless gauge at infinity turns out to be

$$h_+ \pm ih_\times = \mp \frac{1}{\pi r} \int_{-\infty}^{\infty} \frac{d\omega}{\omega} \sum_{l=2}^{\infty} \sum_{m=-l}^l A_{lm\omega} \sqrt{n(n+1)} e^{i\omega(r^*-t)} {}_{\pm 2}Y_{lm}(\theta, \phi), \quad (2.33)$$

where the spin-weighted spherical harmonics ${}_{\pm 2}Y_{lm}$ is defined by

$${}_{\pm 2}Y_{lm}(\theta, \phi) = \frac{1}{2\sqrt{n(n+1)}} \left(W_{lm} \pm \frac{i}{\sin \theta} X_{lm} \right). \quad (2.34)$$

The energy-momentum tensor of the gravitational waves at infinity is given by

$$T_{\mu\nu}^{(\text{GW})} = \frac{1}{32\pi} \left\langle \text{Re}(\nabla_\mu h_{\alpha\beta}^{(\text{TT})}) \text{Re}(\nabla_\nu h^{\alpha\beta(\text{TT})}) \right\rangle, \quad (2.35)$$

in the transverse-traceless gauge, where the angular brackets denote an appropriate average.

From this definition, we find the energy spectrum $dE_{\text{GW}}/d\omega$ of gravitational waves at infinity for the axial mode as

$$\frac{dE_{\text{GW}}}{d\omega} = \frac{1}{32\pi} \sum_{l=2}^{\infty} \sum_{m=-l}^l l(l+1)(l-1)(l+2) |A_{lm\omega}|^2. \quad (2.36)$$

III. GRAVITATIONAL WAVES FROM A SCATTERED TEST PARTICLE

A. Uniform density star

In this subsection, we consider a uniform density star. We restrict our analysis only to the case of the $l = 2$ mode, just for simplicity. We find that features of the energy spectrum of emitted gravitational waves can be classified into two cases, which mainly depend on the shape of the effective potential.

Figure 1 shows the effective potential [Eqs. (2.10) and (2.23)] for a uniform density star with three different compactness parameters R/M . The effective potential has the following three features. First, the Regge-Wheeler potential [Eq. (2.23)] has a maximum point near $r \sim 3M$ (accurately at $r = 3.28M$ for $l = 2$). Second, the potential is discontinuous at the surface because of a discontinuity of the energy density of the star at the surface. Finally, a potential minimum appears inside the star, if the star is ultracompact (for the case of $R \lesssim 3M$).

According to the last feature, we study two cases separately. The first stellar type is the case that the surface is outside the potential barrier ($R \gtrsim 3M$). For a usual neutron star, $R \sim 5M$, and then the first type is most likely a realistic astronomical object. The second stellar type is the case that the surface is inside the potential barrier ($R \lesssim 3M$), which may be an exotic star, if it exists.

First we show our result for the first type. For the case of $R = 5.0M$, we show the energy spectra of emitted gravitational waves in Fig. 2. In this figure, there exists only a single peak in each spectrum. This peak corresponds to the orbital frequency of a test particle at the turning point, i.e., periastron. This means that most gravitational waves are emitted around the turning point, where the effect of the gravitational field is the strongest. No other feature is found in this spectrum. In fact, fixing the energy E and orbital angular momentum L , the spectrum depends less on the compactness parameter R/M (see Fig. 3). For a black hole background, we find quite similar behaviors in the energy spectrum (Fig. 3), except for the high frequency region, where the difference of the boundary conditions is crucial. We also find that the spectrum approaches closer to that of a black hole as the star gets smaller.

We also calculate the waveform for the case of $R = 5.0M$ and black holes, respectively. We see that a burst wave due to the encounter of a test particle emerges for each case. As the same as the energy spectrum, the difference between these waveform is very little (see Fig. 4)

Therefore, for the first stellar type of $R > 3M$, the energy spectrum largely depends on the trajectory, but not on the background object.

Next we discuss an ultracompact star, which shows much more various structure in the spectrum. In this case, a minimum point of the effective potential appears inside the star. As for the trajectory of a test particle, we have two possibilities: one is that the particle gets into the inside region beyond the potential barrier and the other is that one passes through outside the barrier. Since the particle approaches closer to the star, it feels a stronger gravitational field. As a result, the excitation by the particle is more efficient and the emitted gravitational waves are enhanced. As a numerical example, we show those energy spectra for the model with radius $R = 2.26M$ with the turning points $\hat{R}_{\min} = 3.145M$ and $6.628M$ in Fig. 5.

Apart from a global maximum, which appears in the first type model as well and corresponds to the orbital frequency of a test particle at the turning point, we also find many small periodic peaks in Fig. 5. This microscopic peak structure is classified into two types, which are divided at the frequency of the maximum $\omega_{\max} \equiv \sqrt{V_l^{(\text{ext})}_{\max}}$ ($\simeq 0.389M^{-1}$ for $l = 2$) of the effective potential. In the lower frequency region ($\omega < \omega_{\max}$), small and sharp peaks correspond to the quasinormal modes, as we will show it next. For the higher frequency region ($\omega > \omega_{\max}$), we find small periodic peaks, which may appear because of a resonance between two potential barriers. We will also discuss this later.

In order to analyze our numerical results, we first have to know the axial quasinormal modes. Our method to calculate a quasinormal mode is based on the continued fraction expansion method which was originally used for black holes by Leaver [24], and adopted for the polar mode of a spherical star by Leins, Nollert, and Soffel [16]. We apply this method to axial modes as well. We show our results in Table I with those of Kokkotas [20] whose method is different from ours. The table shows that both results agree quite well.

In Fig. 6, we present both the quasinormal mode and energy spectrum. As seen from Fig. 6, axial “quasinormal” modes are classified into two: the lower frequency mode ($\omega < \omega_{\max}$), which imaginary part is very small $\text{Im}(\omega) < O(10^{-8})$, and the higher frequency mode ($\omega > \omega_{\max}$), which imaginary part is rather large $10^{-8} < \text{Im}(\omega) < O(1)$. The reason is very simple. For a frequency lower than ω_{\max} , we can have a quasibound state. Since trapped waves tunnel through the potential barrier, the energy will decrease. It is similar to the quasinormal mode of a black hole. Then, we may call it the axial quasinormal mode as well. However, if the frequency is higher than ω_{\max} , we have no bound state. Nevertheless, we can find the “quasinormal” mode, by which we mean a wave solution with the same boundary condition as that of the conventional quasinormal mode, which is the outgoing wave condition. In the present case, although we find such wave solutions, those waves decay very quickly because the frequency is higher than the potential barrier. This is the reason why we find a large imaginary part of the mode frequency. The solutions which satisfy the boundary condition appear periodically as seen from Fig. 6.

We find that the frequencies of these quasinormal modes coincide with those of spectrum peaks in the frequency region lower than ω_{\max} . This is because a test particle excites those quasinormal modes. In fact, when we see the waveform (Fig. 7), the wave consists of two parts: large one, which corresponds to the burst wave by the encounter by a test particle, and the other part with several oscillations, which comes from excited quasinormal modes in the spectrum. Actually the waveform in the region after $t - r^* \sim 100M$ in Fig. 7 is similar to Kokkotas’s result for a Gaussian pulse wave [25].

On the other hand, in a frequency region higher than ω_{\max} , although many periodic peaks appear, those positions are not exactly the same as the frequencies of “quasinormal” modes. We may understand this fact as follows. Even if the wave frequency ω is higher than the potential barrier, the reflection coefficient does not vanish and oscillates with respect to ω , which period is determined by the potential form. In the present case, we have also an infinite wall near the center of a star. We then expect that small periodic peaks appearing in the spectrum are due to an interference between the incoming and outgoing waves reflected by two potential barriers. Since these waves decay very quickly as mentioned above, the process is quite dynamical, and then the peaks in the spectrum do not coincide with the frequencies of “quasinormal” modes.

In Fig. 8, we show the energy spectra for two stellar models with $R = 2.26M$, and $2.3M$, which correspond to the cases that the turning point is inside and outside the barrier, respectively. For fixed energy E and angular momentum L , the global peaks corresponding to the orbital frequency at the turning point agree with each other. On the other hand, the other small periodic peaks from the excited quasinormal modes do not agree with and rather depend on the compactness parameter R/M . Consequently, from the analysis of the energy spectrum of axial modes, we may determine the compactness parameter R/M of an ultracompact star.

We can also compare a black hole and an ultracompact star. In Fig. 9, we show the energy spectra both for a black hole [8] and an ultracompact star with $R = 2.26M$. From Fig. 9, we see that even for the case of a Schwarzschild black hole, the global peak due to the orbital motion of the particle coincides with that for the star. However, unlike the stellar model, no small periodic peaks appear in the case of a black hole. In fact for a black hole, there is no peak after $t - r^* \sim 100M$ (see Fig. 7). This is because the effective potential of the star has an infinite potential wall near the center, which guarantees the existence of quasinormal modes, while that of a Schwarzschild black hole has no such wall, and incoming waves fall entirely into the event horizon ($r_H = 2M$). Hence, we can also distinguish a

background object, i.e., whether it is an ultracompact star or a black hole, analyzing only axial modes.

As for the total energy of emitted gravitational waves E_{GW} , we find

$$E_{\text{GW}} = \epsilon \frac{\mu^2}{M}, \quad (3.1)$$

with $\epsilon = 2.501 \times 10^{-2}$ and 3.541×10^{-2} for $R = 5M$ and $4M$, respectively, and for $E = 2\mu$ and $L = 12\mu M$. The efficiency ϵ increases monotonically as the compactness gets smaller, and seems to end up with that for Schwarzschild black holes ($\epsilon = 5.687 \times 10^{-2}$). For $E = 1.01\mu$ and $L = 4.5\mu M$, the efficiency, which is $\epsilon \simeq 2.3 \times 10^{-4}$, little depends on R/M up to the case of a black hole.

B. Polytropic star

From the analysis of the energy spectrum for a uniform density star, we find that the spectrum strongly depends on the shape of effective potential. Therefore, it may be important to see the dependence of the equation of state on the energy spectrum. Then, in this section, we study a polytropic star. Just for simplicity, we use the Newtonian polytropic equation of state as

$$P = K\rho^{1+1/n}, \quad (3.2)$$

where n is a polytropic index and K is a constant value.

First, we consider the first type stellar model with $R \gtrsim 3M$. We set the polytropic index $n = 1$ and the constant $K = 100 \text{ km}^2$, and choose the central energy density $\rho_c = 3.0 \times 10^{15} \text{ g/cm}^3$. This choice gives a stellar model with mass $M = 1.267M_\odot$ and radius $R = 8.862 \text{ km}$. The compact parameter is $R/M = 4.739$, and then the surface locates outside the peak of the Regge-Wheeler potential. We show the energy spectra of gravitational waves from a scattering test particle in Fig. 10. We find the same feature as that for the uniform density star with $R \gtrsim 3M$, i.e., there is only a single global peak which frequency corresponds to the orbital one of the particle at the turning point.

Next, we discuss the second type stellar model, i.e., an ultracompact star. To construct an ultracompact star with a polytropic equation of state, we set the polytropic index $n = 0.5$, the constant $K = 100 \text{ km}^4$, and choose the central energy density $\rho_c = 388.097 \times 10^{15} \text{ g/cm}^3$, for which the compactness parameter R/M turns out to be the smallest. For such a choice, the radius, mass, and compactness parameters of the star are $R = 1.136 \text{ km}$, $M = 0.296M_\odot$, and $R = 2.597M$, respectively. Although this seems very implausible for a realistic star, we will use this solution in our analysis to study the dependence of the equation of state on the energy spectrum. In Fig. 11, we show the energy spectra for two trajectories of a test particle. One is the case that a particle goes into the inside of the potential barrier, while the other is the case that a particle passes through only outside the potential barrier. We find the same feature as that of the uniform density star with $R \lesssim 3M$. The difference is found in the frequencies of quasinormal modes because of the different shapes of the potential. Then, we find many small and sharp peaks in the spectrum at the positions different from those for a uniform density star. Consequently, we may be able to distinguish the inside structure of an ultracompact star by observing the energy spectrum of emitted gravitational waves.

IV. CONCLUDING REMARKS

We have studied the axial modes of gravitational waves from a test particle scattered by a spherically symmetric relativistic star. We have considered both a uniform density star and a polytropic star. We find that the energy spectrum depends mainly on the shape of the effective potential for gravitational waves, i.e., whether its minimum exists or not.

When there is no minimum (e.g., a regular type of neutron star with a compactness parameter $R/M \gtrsim 3$), the energy spectrum shows only a single global peak, which corresponds to the orbital frequency of a test particle at the turning point. Gravitational waves are mostly emitted around the turning point, where the effect of the gravitational field is strongest.

While if a minimum of the effective potential exists (i.e., some exotic relativistic star with small compactness parameter $R/M \lesssim 3$), the energy spectrum shows a variety in its structure in addition to the global peak as the same as that found in the previous case. We find small and sharp periodic peaks in the region lower than ω_{max} (the maximum value of the effective potential), which correspond to an excitation of the axial quasinormal modes. The existence of the potential minimum allows the existence of a quasibound state of gravitational waves, i.e., quasinormal modes. Then those modes are excited by a scattered particle. This becomes more conspicuous when the particle gets

into the inside region beyond the potential barrier. We also find small periodic peaks in the frequency region beyond ω_{\max} , which may come from an interference between two waves reflected by the potential barrier and the infinite wall near the center of the star.

From the observation of the energy spectrum of the axial mode, what we can determine? Naively speaking, we may not find any information about the constituent of the star, because the axial mode does not couple to matter fluid. This is true for the first type stellar model, i.e., a regular neutron star. Emitted gravitational waves are mostly determined by the particle orbit. The case of black holes also belongs to this case, although there is a small difference in the high frequency part because of the difference of the boundary condition. However, if a star is compact enough to make a potential minimum ($R \lesssim 3M$), emitted gravitational waves show much more abundant information. It may determine a compactness parameter R/M . We also find quasinormal mode frequencies, which depend on the shape of the potential, and then could depend on the equation of state.

In the axial mode case, however, in general, we cannot have direct information about the matter fluid, in particular about the equation of state. The polar mode of gravitational waves will provide us a more conspicuous dependence of matter property. Work on the polar modes is under way.

ACKNOWLEDGMENTS

We would like to thank Yasufumi Kojima for kind suggestions at the beginning of this study. The Numerical Computations were mainly performed by the FUJITSU-VX vector computer at the Media Network Center, Waseda University. This work was supported partially by a JSPS Grant-in-Aid (No. 5689 and Specially Promoted Research No. 08102010), and by the Waseda University Grant for Special Research Projects.

APPENDIX: NUMERICAL TECHNIQUES SOLVING THE LINEARIZED EINSTEIN EQUATIONS

Here, we present numerical techniques solving the wave equations. We improved Borrelli's method [23] to guarantee numerical accuracy.

For the interior region, the numerical error of the wave function accumulates and becomes maximal at the surface, because the pressure vanishes there. In order to overcome this difficulty, we solve the wave equation both from the center and from the surface, and connect two wave functions at some inner point, e.g., $r = R/2$. For the exterior solution, we integrate the wave equation from the surface to infinity, by which we can reduce the numerical error. In the present model, the test particle mainly emits gravitational waves at the turning point, where we have to solve the wave equation very carefully because an apparent divergence appears. We shall discuss these three methods in order.

1. Interior region of the star

Here we show how to solve the interior wave equation (2.8). Transforming the wave function $X_{l\omega}^{(\text{int})}$ to $Z_{l\omega} = rX_{l\omega}^{(\text{int})}$, we find the perturbation equation for $Z_{l\omega}$ as

$$\frac{d^2 Z_{l\omega}}{dr^2} - \frac{e^\lambda}{r} \left[2 - \frac{6M(r)}{r} - 4\pi r^2 (P - \rho) \right] \frac{dZ_{l\omega}}{dr} + e^{\lambda-\nu} \left(\omega^2 - \frac{2n}{r^2} e^\nu \right) Z_{l\omega} = 0. \quad (\text{A1})$$

From the regularity condition at the center, we obtain the asymptotic behavior at $r \sim 0$ as

$$Z_{l\omega} = \eta_{l\omega} \left\{ r^{l+2} + \frac{1}{2(2l+3)} \left[4\pi(l+2) \left(\frac{1}{3}(2l-1)\rho_c - P_c \right) - \omega^2 e^{-\nu_c} \right] r^{l+4} + O(r^{l+6}) \right\}, \quad (\text{A2})$$

where ρ_c , P_c , and ν_c are density, pressure, and metric functions evaluated at the center, respectively. In order to reduce the numerical error at the surface, we adopt the following procedure.

First, we construct the wave function $Z_{l\omega}^{(0)}$ by integrating Eq. (A1) from the center with the asymptotic behavior, Eq. (A2), to a middle point ($r = R/2$).

Then, we find two independent wave functions $Z_{l\omega}^{(1)}$, $Z_{l\omega}^{(2)}$ by integrating Eq. (A1) from the surface to the middle point. The boundary conditions of those wave functions at the surface are given as $(Z_{l\omega}^{(1)}, dZ_{l\omega}^{(1)}/dr) = (1, 0)$, $(Z_{l\omega}^{(2)}, dZ_{l\omega}^{(2)}/dr) = (0, 1)$. By those two independent solutions, we construct the wave function $Z_{l\omega}(r)$ as

$$Z_{l\omega}(r) = a_{l\omega} Z_{l\omega}^{(1)}(r) + b_{l\omega} Z_{l\omega}^{(2)}(r), \quad (\text{A3})$$

where the coefficients $a_{l\omega}$ and $b_{l\omega}$ are fixed by junction conditions at $r = R/2$. Since the wave functions constructed above must be continuous and smooth at $r = R/2$, we find the junction conditions

$$Z_{l\omega}^{(0)} \left(\frac{R}{2} \right) = a_{l\omega} Z_{l\omega}^{(1)} \left(\frac{R}{2} \right) + b_{l\omega} Z_{l\omega}^{(2)} \left(\frac{R}{2} \right), \quad (\text{A4})$$

$$\frac{dZ_{l\omega}^{(0)}}{dr} \left(\frac{R}{2} \right) = a_{l\omega} \frac{dZ_{l\omega}^{(1)}}{dr} \left(\frac{R}{2} \right) + b_{l\omega} \frac{dZ_{l\omega}^{(2)}}{dr} \left(\frac{R}{2} \right). \quad (\text{A5})$$

From these two conditions, we find $a_{l\omega}$ and $b_{l\omega}$, and then the interior wave function $Z_{l\omega}$.

We finally find values of $X_{l\omega}^{(\text{int})}$ and $dX_{l\omega}^{(\text{int})}/dr^*$ at the surface $r = R$ as

$$X_{l\omega}^{(\text{int})}(R^*) = \frac{1}{R} Z_{l\omega}(R), \quad (\text{A6})$$

$$\frac{dX_{l\omega}^{(\text{int})}}{dr^*}(R^*) = \left(1 - \frac{2M}{R} \right) \left(\frac{1}{R} \frac{dZ_{l\omega}}{dr}(R) - \frac{1}{R^2} Z_{l\omega}(R) \right), \quad (\text{A7})$$

where R^* is the tortoise coordinate of the surface R .

2. Exterior region of the star

Next we construct the exterior wave function. In order to use the Green's function method, we first consider the homogeneous wave function $X_{lm\omega}^{(\text{ext})(0)}$, which satisfies the wave equation

$$\frac{d^2 X_{lm\omega}^{(\text{ext})(0)}}{dr^{*2}} + \left(\omega^2 - V_l^{(\text{ext})} \right) X_{lm\omega}^{(\text{ext})(0)} = 0, \quad (\text{A8})$$

and the boundary condition at the surface, which we have already evaluated in the previous subsection, that is,

$$X_{lm\omega}^{(\text{ext})(0)}(R^*) = X_{l\omega}^{(\text{int})}(R^*), \quad (\text{A9})$$

$$\frac{dX_{lm\omega}^{(\text{ext})(0)}}{dr^*}(R^*) = \frac{dX_{l\omega}^{(\text{int})}}{dr^*}(R^*). \quad (\text{A10})$$

Then, we construct a particular solution $X_{lm\omega}^{(\text{ext})(1)}$ with a source term, which equation is described as

$$\frac{d^2 X_{lm\omega}^{(\text{ext})(1)}}{dr^{*2}} + \left(\omega^2 - V_l^{(\text{ext})} \right) X_{lm\omega}^{(\text{ext})(1)} = S_{lm\omega}^{(\text{ext})}, \quad (\text{A11})$$

where $S_{lm\omega}^{(\text{ext})}$ comes from the motion of a test particle. At the surface, the solution $X_{lm\omega}^{(\text{ext})(1)}$ satisfies the following condition:

$$X_{lm\omega}^{(\text{ext})(1)}(R^*) = 0, \quad (\text{A12})$$

$$\frac{dX_{lm\omega}^{(\text{ext})(1)}}{dr^*}(R^*) = 0. \quad (\text{A13})$$

For the homogeneous equation (A8), we have two independent solutions $u_{lm\omega}^{(\text{out})}(r^*)$ and $u_{lm\omega}^{(\text{in})}(r^*)$, which correspond to outgoing and incoming waves at infinity, respectively. Then, we describe the wave function $X_{lm\omega}^{(\text{ext})(0)}$ by these two independent solutions as

$$X_{lm\omega}^{(\text{ext})(0)}(r^*) = \alpha_{lm\omega} u_{lm\omega}^{(\text{out})}(r^*) + \beta_{lm\omega} u_{lm\omega}^{(\text{in})}(r^*), \quad (\text{A14})$$

where $\alpha_{lm\omega}$ and $\beta_{lm\omega}$ are complex constants, which are fixed by Eqs. (A9), (A10).

The Green's function $G(r^*, s^*)$ for Eq. (A11) is also constructed by $u_{lm\omega}^{(\text{out})}$ and $u_{lm\omega}^{(\text{in})}$ as

$$G(r^*, s^*) = \frac{1}{W} \left[-u^{(\text{out})}(r^*)u^{(\text{in})}(s^*) + u^{(\text{in})}(r^*)u^{(\text{out})}(s^*) \right] \theta(r^* - s^*) \quad (r^* > s^*), \quad (\text{A15})$$

where W is the Wronskian and $\theta(x)$ is the Heaviside function. The wave function $X_{lm\omega}^{(\text{ext})(1)}$ is obtained by integration as

$$X_{lm\omega}^{(\text{ext})(1)}(r^*) = \int_{R^*}^{\infty} G(r^*, s^*) S_{lm\omega}^{(\text{ext})}(s^*) ds^*. \quad (\text{A16})$$

Then, the solution for the exterior wave equation (2.21) with the same boundary conditions as Eqs. (A9), (A10) is given as

$$X_{lm\omega}^{(\text{ext})}(r^*) = \alpha_{lm\omega} u_{(\text{out})}(r^*) + \beta_{lm\omega} u_{(\text{in})}(r^*) + \int_{R^*}^{\infty} G(r^*, s^*) S_{lm\omega}^{(\text{ext})}(s^*) ds^*. \quad (\text{A17})$$

The asymptotic behavior of $X_{lm\omega}^{(\text{ext})}(r^*)$ as $r \rightarrow \infty$ is given by

$$X_{lm\omega}^{(\text{ext})}(r^*) \rightarrow (\alpha_{lm\omega} + \rho_{lm\omega}) e^{i\omega r^*} + (\beta_{lm\omega} + \sigma_{lm\omega}) e^{-i\omega r^*} \quad (r^* \rightarrow \infty), \quad (\text{A18})$$

where $\rho_{lm\omega}$ and $\sigma_{lm\omega}$ are defined by

$$\rho_{lm\omega} = -\frac{1}{W} \int_{R^*}^{\infty} u_{lm\omega}^{(\text{in})}(s^*) S_{lm\omega}^{(\text{ext})}(s^*) ds^*, \quad (\text{A19})$$

$$\sigma_{lm\omega} = \frac{1}{W} \int_{R^*}^{\infty} u_{lm\omega}^{(\text{out})}(s^*) S_{lm\omega}^{(\text{ext})}(s^*) ds^*. \quad (\text{A20})$$

Since there is no incoming wave, we find the boundary condition such that

$$\beta_{lm\omega} + \sigma_{lm\omega} = 0. \quad (\text{A21})$$

Then, the amplitude $A_{lm\omega}$ of gravitational waves at infinity is given by

$$A_{lm\omega} = \alpha_{lm\omega} + \rho_{lm\omega}. \quad (\text{A22})$$

In order to extract the amplitude $A_{lm\omega}$ from our solution, we use the relation

$$\begin{aligned} -\beta_{lm\omega} \rho_{lm\omega} + \alpha_{lm\omega} \sigma_{lm\omega} &= \frac{1}{W} \int_{R^*}^{\infty} \left[\alpha_{lm\omega} u_{lm\omega}^{(\text{out})}(s^*) + \beta_{lm\omega} u_{lm\omega}^{(\text{in})}(s^*) \right] S_{lm\omega}^{(\text{ext})}(s^*) ds^* \\ &= \frac{1}{W} \int_{R^*}^{\infty} X_{lm\omega}^{(\text{ext})(0)}(s^*) S_{lm\omega}^{(\text{ext})}(s^*) ds^*. \end{aligned} \quad (\text{A23})$$

With Eqs. (A21) and (A23), we finally obtain the amplitude as

$$A_{lm\omega} = \alpha_{lm\omega} + \rho_{lm\omega} = -\frac{1}{\beta_{lm\omega}} \frac{1}{W} \int_{R^*}^{\infty} X_{lm\omega}^{(\text{ext})(0)}(s^*) S_{lm\omega}^{(\text{ext})}(s^*) ds^*, \quad (\text{A24})$$

where $\beta_{lm\omega}$ is already obtained up to an unknown constant $\eta_{l\omega}$, which is canceled out with that of $X_{lm\omega}^{(\text{ext})(0)}$ in Eq. (A24)

3. Numerical method to integrate near the turning point of a test particle orbit

When a test particle is scattered by a star, the orbit includes a turning point (\hat{R}_{min} or \hat{R}_{min}^* by the tortoise coordinate), where the radial velocity $d\hat{R}/d\tau$ vanishes. The source term $S_{lm\omega}^{(\text{ext})}$ in Eq. (A24) is given by Eq. (2.24), where $Q_{lm}(\omega, r)$ and $D_{lm}(\omega, r)$, defined by Eqs. (2.25) and (2.26), for the present orbit ($\hat{\Theta} = \pi/2$) are described as

$$\begin{aligned} Q_{lm}(\omega, r) &= -C_{lm} \sqrt{\frac{2}{l(l+1)}} \frac{\mu}{r(1-2M/r)} \int_{-\infty}^{\infty} d\tau \frac{d\hat{R}}{d\tau} \delta(r - \hat{R}(\tau)) \\ &\quad \times \frac{\tilde{L}}{\hat{R}^2} \frac{dP_{lm}}{d\hat{\Theta}} \left(\frac{\pi}{2} \right) e^{i(\omega\hat{T} - m\hat{\Phi})}, \end{aligned} \quad (\text{A25})$$

$$D_{lm}(\omega, r) = \frac{-imC_{lm}}{\sqrt{2n(n+1)}} \mu \int_{-\infty}^{\infty} d\tau \delta(r - \hat{R}(\tau)) \frac{\tilde{L}^2}{\hat{R}^4} \frac{dP_{lm}}{d\hat{\Theta}} \left(\frac{\pi}{2} \right) e^{i(\omega\hat{T} - m\hat{\Phi})}, \quad (\text{A26})$$

where

$$C_{lm} = (-1)^{(m+|m|)/2} \sqrt{\frac{(2l+1)(l-|m|)!}{4\pi(l+|m|)!}}, \quad (\text{A27})$$

which is a normalization constant of a spherical harmonics Y_{lm} , and $P_{lm}(\cos\theta)$ is the associated Legendre function.

Integration over the proper time τ gives the term of $(d\hat{R}/d\tau)^{-1}$ in Eq. (A26), which diverges at the turning point, and then the integration

$$\frac{1}{W} \int_{R^*}^{\infty} X_{lm\omega}^{(\text{ext})(0)}(s^*) S_{lm\omega}^{(\text{ext})}(s^*) ds^* = \frac{1}{W} \int_{\hat{R}_{\text{min}}^*}^{\infty} X_{lm\omega}^{(\text{ext})(0)}(s^*) S_{lm\omega}^{(\text{ext})}(s^*) ds^* \quad (\text{A28})$$

diverges apparently. However, this is not a physical divergence, but rather comes from the change of integration variables from the proper time τ to the radius r . This transformation becomes singular at the turning point because $d\hat{R}/d\tau = 0$. In order to avoid this difficulty, we shall use a time coordinate \hat{T} in the integration.

Since the trajectory before and after the turning point is symmetric, we choose the initial position of the particle $\hat{T} = 0$, $\hat{\Phi} = 0$ at the turning point and integrate from there to infinity. The integral, Eq. (A28), is then written as

$$\frac{1}{W} \int_{\hat{R}_{\min}}^{\infty} ds^* X_{lm\omega}^{(\text{ext})(0)} S_{lm\omega}^{(\text{ext})}(s^*) = \frac{1}{W} \int_0^{\infty} d\hat{T} \left[X_{lm\omega}^{(\text{ext})(0)}(\hat{T}) \left[S_{lm}^{(0)}(\hat{T}) + S_{lm}^{(1)}(\hat{T}) \right] + \hat{R} \left(1 - \frac{2M}{\hat{R}} \right) \frac{1}{d\hat{R}/d\hat{T}} \frac{dX_{lm\omega}^{(\text{ext})(0)}}{d\hat{T}} S_{lm}^{(1)}(\hat{T}) \right], \quad (\text{A29})$$

$$\hat{S}_{lm}^{(0)} = \frac{8\pi}{\tilde{E}} \left[\sqrt{\frac{2}{l(l+1)}} \left(1 - \frac{2M}{\hat{R}} \right)^2 \hat{Q}_{lm} + \sqrt{\frac{2}{l(l+1)(l-1)(l+2)}} \frac{2M}{\hat{R}} \left(1 - \frac{2M}{\hat{R}} \right) \hat{D}_{lm} \right], \quad (\text{A30})$$

$$\hat{S}_{lm}^{(1)} = -\frac{8\pi}{\tilde{E}} \sqrt{\frac{2}{l(l+1)(l-1)(l+2)}} \left(1 - \frac{2M}{\hat{R}} \right) \hat{D}_{lm}, \quad (\text{A31})$$

$$\hat{Q}_{lm} = -2iC_{lm} \sqrt{\frac{2}{l(l+1)}} \frac{\mu \tilde{L}}{\hat{R}^3 (1 - 2M/\hat{R})} \gamma^{1/2} \frac{dP_{lm}}{d\hat{\Theta}} \left(\frac{\pi}{2} \right) \sin(\omega\hat{T} - m\hat{\Phi}), \quad (\text{A32})$$

$$\hat{D}_{lm} = \frac{-4imC_{lm}}{\sqrt{2l(l+1)(l-1)(l+2)}} \frac{\mu \tilde{L}^2}{\hat{R}^4} \frac{dP_{lm}}{d\hat{\Theta}} \left(\frac{\pi}{2} \right) \cos(\omega\hat{T} - m\hat{\Phi}), \quad (\text{A33})$$

where $X_{lm\omega}^{(\text{ext})(0)}(\hat{T}) = X_{lm\omega}^{(\text{ext})(0)}(\hat{R}(\hat{T}))$ and $dX_{lm\omega}^{(\text{ext})(0)}/d\hat{T}$ is its time derivative. However, the term in Eq. (A29),

$$\frac{1}{d\hat{R}/d\hat{T}} \frac{dX_{lm\omega}^{(\text{ext})(0)}}{d\hat{T}} = \frac{dX_{lm\omega}^{(\text{ext})(0)}}{d\hat{R}}, \quad (\text{A34})$$

is still apparently divergent because $d\hat{R}/d\hat{T}$ vanishes at the turning point.

To avoid this difficulty, we expand $X_{lm\omega}^{(\text{ext})(0)}$, $dX_{lm\omega}^{(\text{ext})(0)}/d\hat{R}$ near the turning point. From the equation of motion, we find

$$\frac{d\hat{R}}{d\hat{T}} \propto (\hat{R} - \hat{R}_{\min})^{1/2} + O(\hat{R} - \hat{R}_{\min}), \quad (\text{A35})$$

which is integrated as

$$\hat{R} - \hat{R}_{\min} = a_0 \hat{T}^2 + O(\hat{T}^4), \quad (\text{A36})$$

where a_0 is an integration constant. Then, we find the wave function near the turning point as

$$\begin{aligned} X_{lm\omega}^{(\text{ext})(0)} &= X_{lm\omega}^{(\text{ext})(0)}(\hat{R}_{\min}) + \frac{dX_{lm\omega}^{(\text{ext})(0)}}{dr}(\hat{R}_{\min}) (\hat{R} - \hat{R}_{\min}) \\ &= X_{lm\omega}^{(\text{ext})(0)}(\hat{R}_{\min}) + \frac{a_0}{1 - 2M/\hat{R}_{\min}} \frac{dX_{lm\omega}^{(\text{ext})(0)}}{dr^*}(\hat{R}_{\min}^*) \hat{T}^2, \end{aligned} \quad (\text{A37})$$

$$\begin{aligned} \frac{dX_{lm\omega}^{(\text{ext})(0)}}{d\hat{R}} &= \frac{dX_{lm\omega}^{(\text{ext})(0)}}{dr}(\hat{R}_{\min}) + \frac{d^2 X_{lm\omega}^{(\text{ext})(0)}}{dr^2}(\hat{R}_{\min}) (\hat{R} - \hat{R}_{\min}) \\ &= \frac{1}{1 - 2M/\hat{R}_{\min}} \frac{dX_{lm\omega}^{(\text{ext})(0)}}{dr^*}(\hat{R}_{\min}^*) \\ &\quad + \frac{a_0}{(1 - 2M/\hat{R}_{\min})^2} \left(-\frac{2M}{\hat{R}_{\min}^2} \frac{dX_{lm\omega}^{(\text{ext})(0)}}{dr^*}(\hat{R}_{\min}^*) + \frac{d^2 X_{lm\omega}^{(\text{ext})(0)}}{dr^{*2}}(\hat{R}_{\min}^*) \right) \hat{T}^2, \end{aligned} \quad (\text{A38})$$

where $X_{lm\omega}^{(\text{ext})(0)}$, $dX_{lm\omega}^{(\text{ext})(0)}/dr^*$, and $d^2 X_{lm\omega}^{(\text{ext})(0)}/dr^{*2}$ at the turning point \hat{R}_{\min}^* are found easily by integration of Eq. (A8). Since those functions are regular at the turning point, we can evaluate Eq. (A29) without any difficulty.

- [1] See, for example, A. Abramovici *et al.*, Science **256**, 325 (1992), for LIGO; C. Bradaschia *et al.*, Nucl. Instrum. Methods Phys. Res. A **289**, 518 (1990), for VIRGO; J. Hough, in *Proceedings of the Sixth Marcel Grossmann Meeting*, edited by H. Sato and T. Nakamura (World Scientific, Singapore, 1992), p. 192, for GEO600; K. Kuroda *et al.*, in *Proceedings of International Conference on Gravitational Waves: Sources and Detectors*, edited by I. Ciufolini and F. Fiducaro (World Scientific, Singapore, 1997), p. 100, for TAMA300.
- [2] P. Anninos, D. Hobill, E. Seidel, L. Smarr, and W.-M. Suen, Phys. Rev. D **52**, 2044 (1995) ; Phys. Rev. Lett. **71**, 2851 (1993).
- [3] P. Anninos and S. Brandt, Phys. Rev. Lett. **81**, 508 (1998).
- [4] T. Regge and J. A. Wheeler, Phys. Rev. **108**, 1063 (1957).
- [5] F. J. Zerilli, Phys. Rev. D **2**, 2141 (1970).
- [6] M. Davis, R. Ruffini, and J. Tiomno, Phys. Rev. D **5**, 2932 (1972).
- [7] K. Oohara and T. Nakamura, Prog. Theor. Phys. **70**, 757 (1983).
- [8] K. Oohara and T. Nakamura, Prog. Theor. Phys. **71**, 91 (1984).
- [9] P. Anninos, R. H. Price, J. Pullin, E. Seidel, and W.-M. Suen, Phys. Rev. D **52**, 4462 (1995).
- [10] K. S. Thorne and A. Campolattaro, Astrophys. J. **149**, 591 (1967); **152**, 673 (1967).
- [11] L. Lindblom and S. Detweiler, Astrophys. J., Suppl. Ser. **53**, 73 (1983); S. Detweiler and L. Lindblom, Astrophys. J. **292**, 12 (1985).
- [12] L. Lindblom, G. Mendell, and J. R. Ipser, Phys. Rev. D **56**, 2118 (1997).
- [13] E. Balbinski, S. Detweiler, L. Lindblom, and B. F. Schutz, Mon. Not. R. Astron. Soc. **213**, 553 (1985).
- [14] Y. Kojima, Prog. Theor. Phys. **79**, 665 (1988).
- [15] K. D. Kokkotas and B. F. Schutz, Mon. Not. R. Astron. Soc. **255** 119 (1992).
- [16] M. Leins, H. -P. Nollert, and M. H. Soffel, Phys. Rev. D **48**, 3467 (1993).
- [17] N. Andersson, K. D. Kokkotas, and B. F. Schutz, Mon. Not. R. Astron. Soc. **274**, 1039 (1995).
- [18] N. Andersson, Y. Kojima, and K. D. Kokkotas, Astrophys. J. **462**, 855 (1996).
- [19] S. Chandrasekhar and V. Ferrari, Proc. R. Soc. London **A432**, 247 (1991) ; **A434**, 449 (1991).
- [20] K. D. Kokkotas, Mon. Not. R. Astron. Soc. **268**, 1015 (1994); **277**, 1599 (1995).
- [21] Y. Kojima, Phys. Rev. D **46**, 4289 (1992).
- [22] Y. Kojima, Prog. Theor. Phys. **77**, 297 (1987).
- [23] A. Borrelli, Nuovo Cimento B **112**, 225 (1997).
- [24] E. W. Leaver, Proc. R. Soc. London **A402**, 285 (1985).
- [25] K. D. Kokkotas, in *Proceedings of Relativistic Gravitation and Gravitational Radiation*, edited by J.-A. Marck and J.-P. Lasota (Cambridge University Press, Cambridge, England, 1997), p. 89.

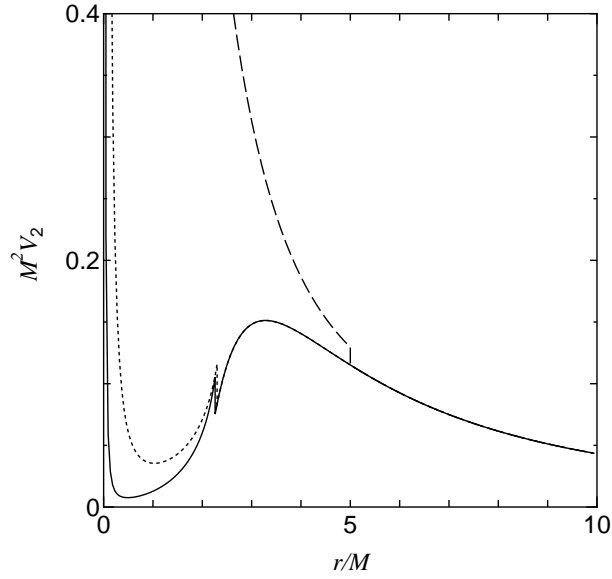


FIG. 1. Effective potentials of a uniform density star for the $l = 2$ mode. Solid, dotted, and dashed lines correspond to stellar models with radius $R = 2.26M$, $2.3M$, and $5.0M$, respectively. For an ultracompact star ($R < 3M$), the potential has a minimum, which traps gravitational waves emitted by a test particle.

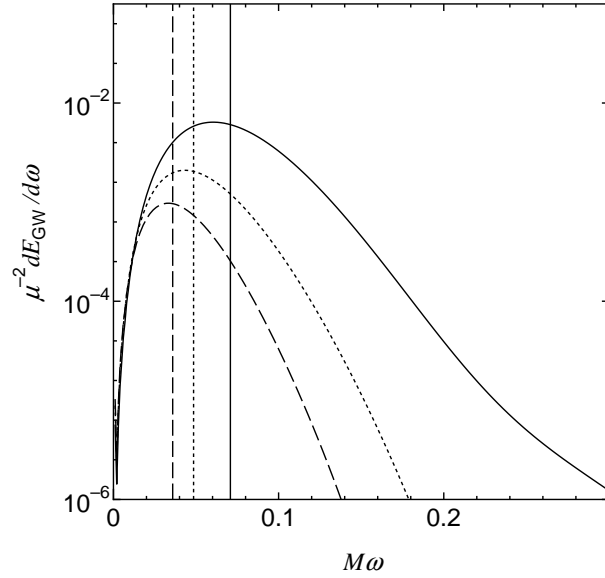


FIG. 2. The energy spectrum ($l = 2$ mode) of gravitational waves from a test particle with $E = 1.01\mu$ scattered by a uniform density star with $R = 5.0M$. Solid, dotted, and dashed lines show the cases of the angular momentum $L = 4.5\mu M$, $5.0\mu M$, and $5.5\mu M$, respectively. Longitudinal lines represent the frequency of a test particle at the turning point. Peaks correspond to orbital frequencies at the turning point of a test particle.

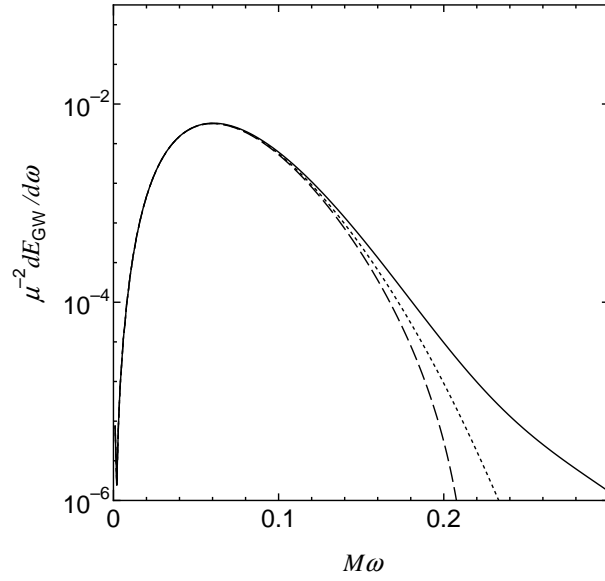


FIG. 3. The energy spectrum ($l = 2$ mode) of gravitational waves for a uniform density star with $R = 5.0M$ and for a Schwarzschild black hole. We choose the energy and angular momentum of the test particle as $(E, L) = (1.01\mu, 4.5\mu M)$. Solid, dotted, and dashed lines correspond to the cases of the uniform density star with $R = 5.0M$, $4.0M$, and of a Schwarzschild black hole, respectively. The peak in the spectrum coincides each other because of the same trajectory of the test particle.

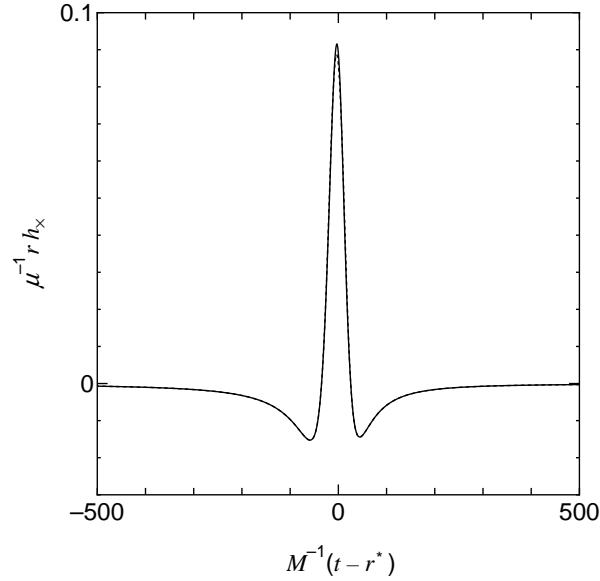


FIG. 4. Waveforms observed in the direction of $\theta = \pi/2$, $\phi = 0$ ($l = 2$ mode) for a uniform density star with $R = 5.0M$ (solid line) and for a Schwarzschild black hole (dotted line). We set the energy and angular momentum of the test particle as $(E, L) = (1.01\mu, 4.5\mu M)$. In this case, the $+$ mode cancels out in the waveform.

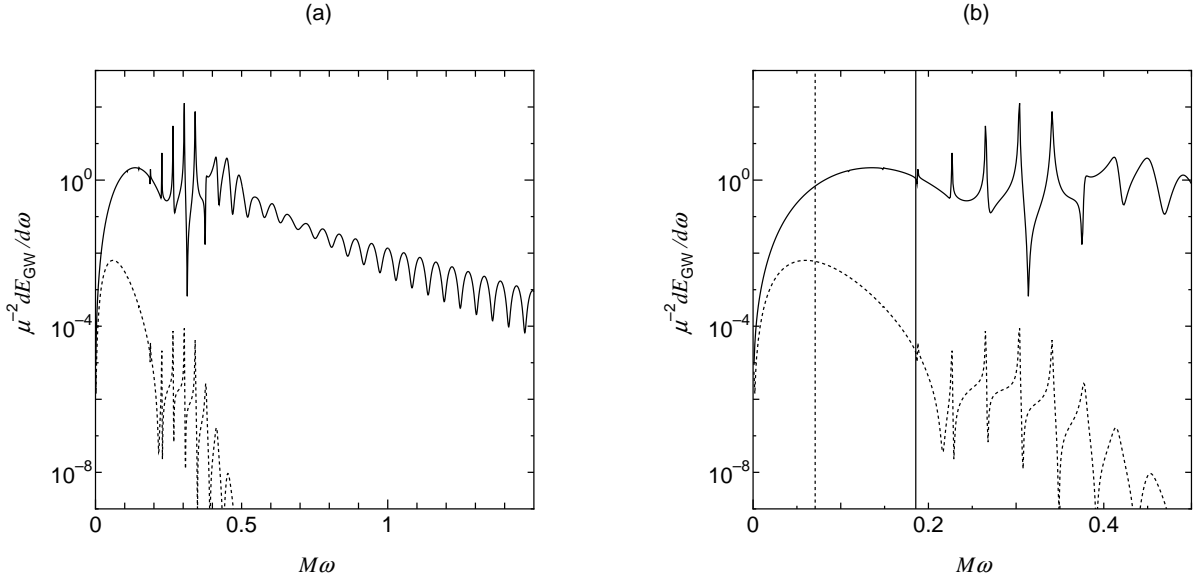


FIG. 5. The energy spectrum ($l = 2$ mode) of gravitational waves for the case of a uniform density star with $R = 2.26M$. Solid and dotted lines correspond to $(E, L) = (2.38\mu, 12.0\mu M)$ and $(1.01\mu, 4.5\mu M)$, respectively. (b) is an enlargement of (a) to show the resonant peaks in detail. Longitudinal lines represent the frequency of a test particle at the turning point. We find some periodic peaks, which never appear in Fig. 2. Those small periodic peaks are classified into two types: one for $\omega < \omega_{\max}$ and the other for $\omega > \omega_{\max}$, where ω_{\max} corresponds to the maximum energy of the effective potential in Fig. 1.

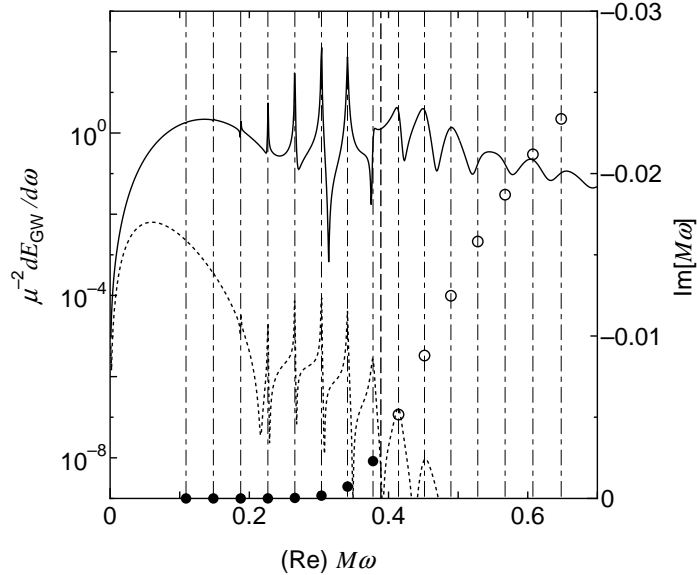


FIG. 6. The energy spectrum ($l = 2$ mode) of gravitational waves and axial “quasinormal” modes for the case of a uniform density star with $R = 2.26M$. Solid and dotted lines correspond to $(E, L) = (2.38\mu, 12.0\mu M)$ and $(1.01\mu, 4.5\mu M)$, respectively, which are the same those in Fig. 5. A longitude dash line represents the frequency of the maximum ω_{\max} of the effective potential. Solid ($\omega < \omega_{\max}$) and open ($\omega > \omega_{\max}$) circles denote axial “quasinormal” modes of the uniform density star with $R = 2.26M$. We find that resonant periodic peaks for $\omega < \omega_{\max}$ agree quite well with those quasinormal modes, which are excited by a scattered test particle. However, small periodic peaks for $\omega > \omega_{\max}$ seem not coincide exactly with “quasinormal” modes.

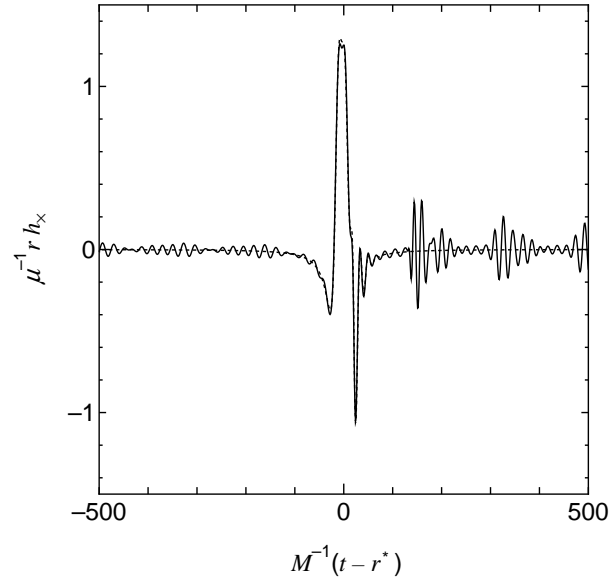


FIG. 7. The waveform observed in the direction of $\theta = \pi/2$, $\phi = 0$ ($l = 2$ mode) for a uniform density star with $R = 2.26M$ (solid line) and for a Schwarzschild black hole (dotted line). We set the energy and angular momentum of the test particle as $(E, L) = (2.38\mu, 12.0\mu M)$. In this case, the + mode cancels out in the waveform.

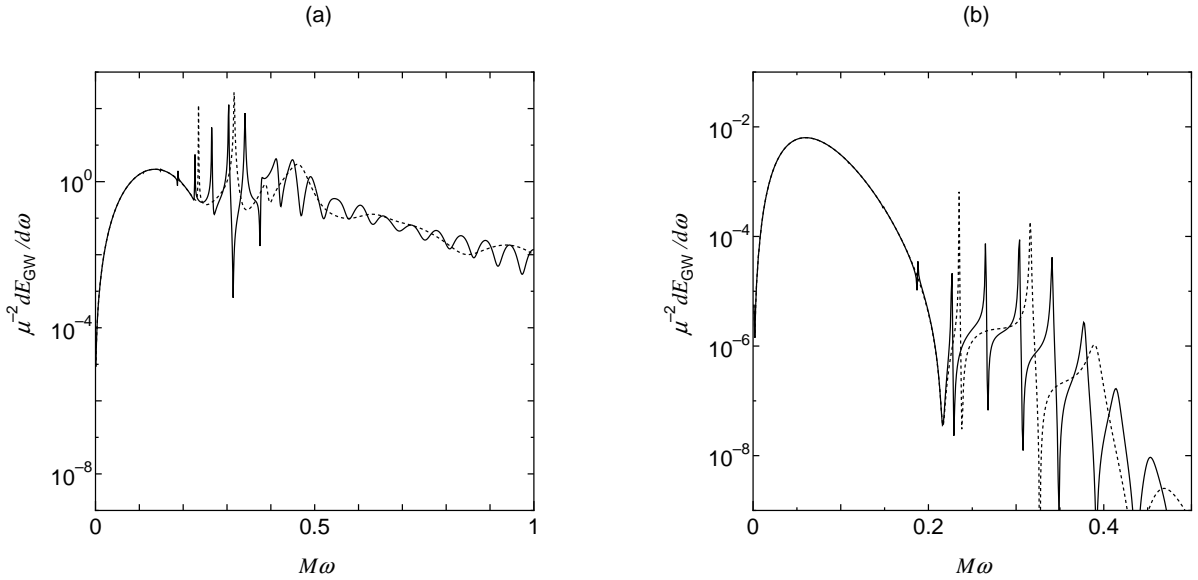


FIG. 8. The energy spectrum ($l = 2$ mode) of gravitational waves for uniform density stars with two different compactness parameters, $R = 2.26M$ (solid line) and $2.3M$ (dotted line). We set the energy and angular momentum of the test particle as (a) $(E, L) = (2.38\mu, 12.0\mu M)$ and (b) $(E, L) = (1.01\mu, 4.5\mu M)$. Although global peaks coincide with each other because of the same trajectory of the particle, resonant periodic peaks are different because of the different compactness. This may show us how to distinguish the compactness of a star by use of observational data.

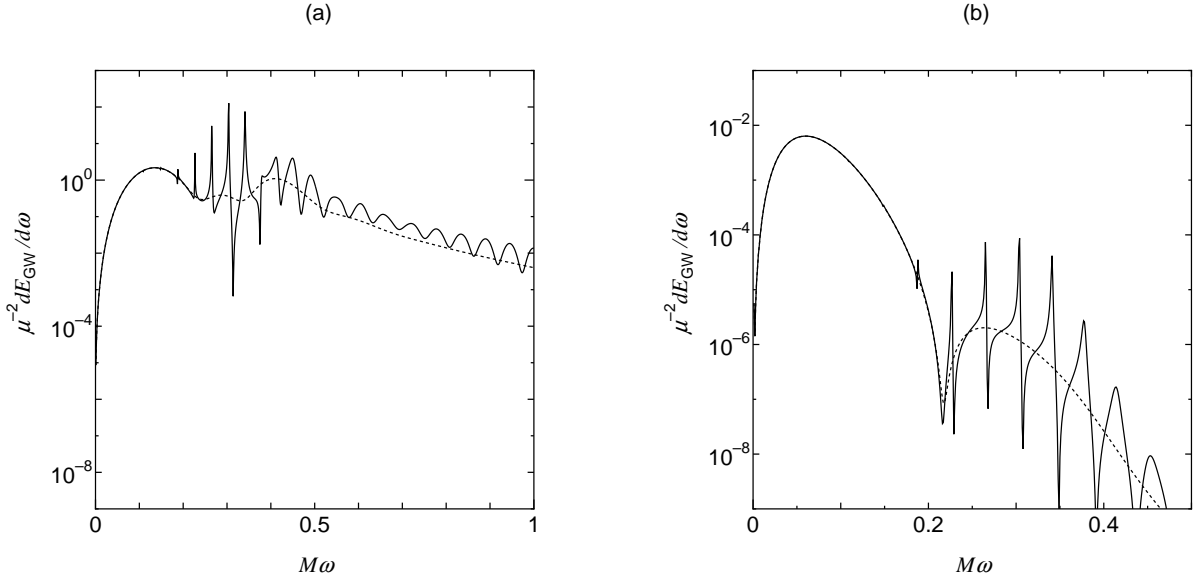


FIG. 9. The energy spectra ($l = 2$ mode) of gravitational waves for a uniform density star with $R = 2.26M$ (solid line) and for a Schwarzschild black hole (dotted line). We set the energy and angular momentum of the test particle as (a) $(E, L) = (2.38\mu, 12.0\mu M)$ and (b) $(E, L) = (1.01\mu, 4.5\mu M)$. This difference may enable us to distinguish an ultracompact star from a black hole.

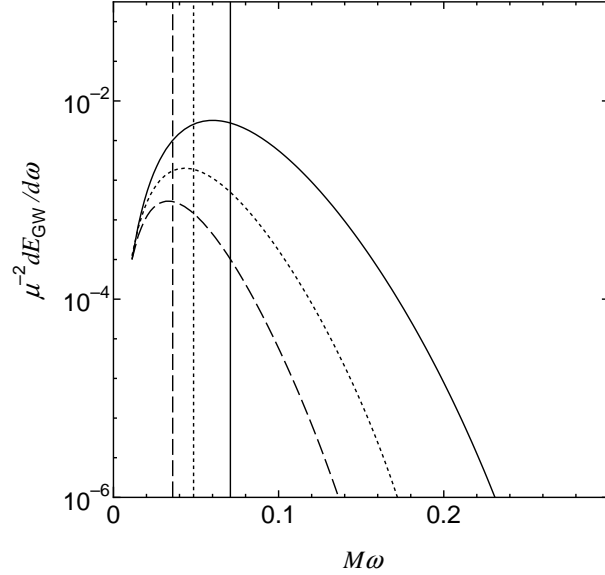


FIG. 10. The energy spectrum ($l = 2$ mode) of gravitational waves for the case of the polytropic star with a large compactness parameter. We set the polytropic index $n = 1$, the center of the density $\rho_c = 3.0 \times 10^{15} \text{ g / cm}^3$, and the energy of the test particle as $E = 1.01\mu$. The solid, dotted, and dashed lines correspond to the angular momentum of the test particle $L = 4.5\mu M$, $5.0\mu M$, and $5.5\mu M$, respectively. Longitudinal lines represent the frequency of a test particle at the turning point. This figure shows the same feature as Fig. 2.

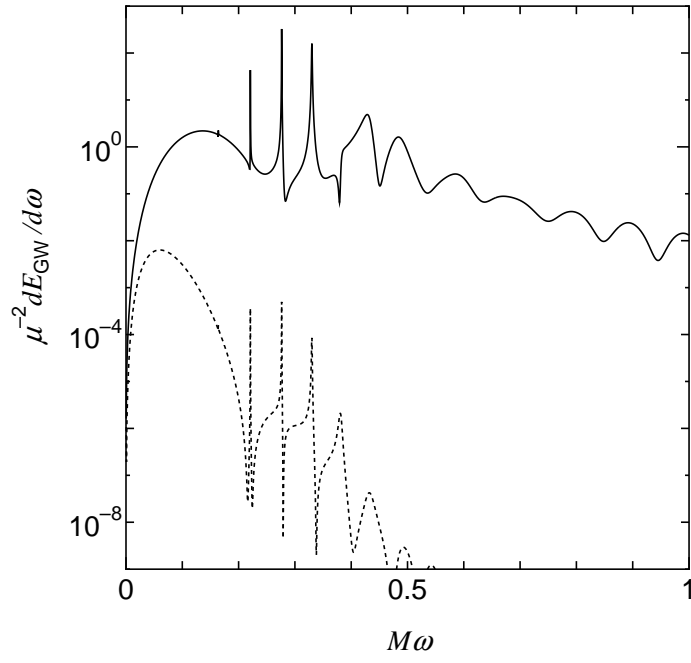


FIG. 11. The energy spectrum ($l = 2$ mode) of the gravitational waves for the case of the polytropic star with a small compactness parameter. We set the polytropic index $n = 0.5$ and the center of the density $\rho_c = 388.097 \times 10^{15} \text{ g / cm}^3$, which may be implausible but is necessary to obtain an ultracompact star. The solid and dotted lines correspond to $(E, L) = (2.38\mu, 12.0\mu M)$ and $(1.01\mu, 4.5\mu M)$, respectively. This figure shows the same features as Fig. 5.

TABLE I. Axial “quasinormal” modes for a uniform density star with $R = 2.26M$. We use the continued fraction expansion method, which was first used to calculate black hole quasinormal modes by Leaver [24], and w modes of a polytropic star by Leins, Nollert, and Soffel [16]. Our results agree quite well with those of Kokkotas, who adopted a different method [20]. Our imaginary part has opposite sign to Kokkotas’s result, because our definition of the Fourier transformation is opposite to his.

Our results		Kokkotas’s results	
Re[$M\omega$]	-Im[$M\omega$]	Re[$M\omega$]	Im[$M\omega$]
0.1090	1.2399×10^{-9}	0.1091	1.2388×10^{-9}
0.1484	3.9495×10^{-8}	0.1484	3.9494×10^{-8}
0.1876	5.4678×10^{-7}	0.1876	5.4701×10^{-7}
0.2267	4.8526×10^{-6}	0.2267	4.8528×10^{-6}
0.2654	3.2318×10^{-5}	0.2654	3.2316×10^{-5}
0.3036	1.7234×10^{-4}	0.3036	1.7236×10^{-4}
0.3410	7.3017×10^{-4}	0.3411	7.3003×10^{-4}
0.3777	2.2982×10^{-3}	0.3777	2.2982×10^{-3}
0.4144	5.1672×10^{-3}	0.4144	5.1490×10^{-3}
0.4516	8.7987×10^{-3}	0.4516	8.7685×10^{-3}
0.4896	1.2480×10^{-2}	0.4896	1.2490×10^{-2}
0.5282	1.5818×10^{-2}	0.5282	1.5804×10^{-2}
0.5674	1.8702×10^{-2}	0.5675	1.8710×10^{-2}
0.6074	2.1187×10^{-2}	0.6074	2.1208×10^{-2}
0.6481	2.3368×10^{-2}	0.6481	2.3349×10^{-2}